Impact of liver-specific survival motor neuron (SMN) depletion on central nervous system and peripheral tissue pathology

Monique Marylin Alves de Almeida[1,2], Yves De Repentigny[1], Sabrina Gagnon[1], Emma R. Sutton[1,2], Rashmi Kothary[1,2,3,4*]

[1]Regenerative Medicine Program, Ottawa Hospital Research Institute, Ottawa, K1H 8L6, Canada
[2]Centre for Neuromuscular Disease, University of Ottawa, K1H 8M5, Canada
[3]Department of Cellular and Molecular Medicine, University of Ottawa, Ottawa, K1H 8M5, Canada
[4]Department of Medicine, University of Ottawa, Ottawa, K1H 8M5, Canada
*Corresponding author: rkothary@ohri.ca

Abstract

Spinal muscular atrophy (SMA) is an inherited neuromuscular disorder stemming from deletions or mutations in the Survival Motor Neuron 1 (*SMN1*) gene, leading to decreased levels of SMN protein, and subsequent motor neuron death and muscle atrophy. While traditionally viewed as a disorder predominantly affecting motor neurons, recent research suggests the involvement of various peripheral organs in SMA pathology. Notably, the liver has emerged as a significant focus due to the observed fatty liver phenotype and dysfunction in both SMA mouse models and SMA patients. Despite these findings, it remains unclear whether intrinsic depletion of SMN protein in the liver contributes to pathology in the peripheral or central nervous systems. To address this knowledge gap, we developed a mouse model with a liver-specific depletion of SMN by utilizing an *Alb-Cre* transgene together with one Smn^{2B} allele and one *Smn* exon 7 allele flanked by loxP sites. Initially, we evaluated phenotypic changes in these mice at postnatal day 19 (P19), a time when the severe model of SMA, the $Smn^{2B/-}$ mice, typically exhibit many symptoms of the disease. Our findings indicate that liver-specific SMN depletion does not induce motor neuron death, neuromuscular pathology or muscle atrophy, characteristics typically observed in the $Smn^{2B/-}$ mouse at P19. However, mild liver steatosis was observed at this time point, although no changes in liver function were detected. Notably, pancreatic alterations resembled that of $Smn^{2B/-}$mice, with a decrease in insulin-producing β-cells and an increase in glucagon-producing α-cells, accompanied by a reduction in blood glucose and an increase in plasma glucagon and glucagon-like peptide (GLP-1) levels. Moreover, these changes were transient, as P60 mice exhibited recovery of liver and pancreatic function. While the mosaic pattern of the Cre-mediated excision precludes definitive conclusions regarding the contribution of liver-specific SMN depletion to overall tissue pathology, our findings highlight an intricate connection between liver function and pancreatic abnormalities in SMA, adding a nuanced layer to our understanding of the disease's complexities.

Keywords
Spinal muscular atrophy, neuromuscular disease, metabolism, pancreas

1. Introduction

Insufficient levels of Survival Motor Neuron (SMN) protein, primarily arising from mutations or deletions in the *SMN1* gene, are the root cause of spinal muscular atrophy (SMA), a hereditary neuromuscular disorder widely acknowledged as one of the leading genetic causes of infant mortality[1-3]. Characterized by the loss of motor neurons, SMA presents as a progressive weakening of muscle strength, primarily impacting proximal muscles. If left untreated, this deterioration culminates in respiratory failure and premature mortality[4].

The diverse phenotypes observed in SMA patients can be attributed to the genetic variations within the *SMN* gene[1]. Humans harbor two copies of the *SMN* gene, *SMN1* and *SMN2*, which share a nearly identical sequence except for a critical C to T substitution at position 6 of exon 7 in *SMN2*[5]. This single nucleotide change disrupts splicing of the gene, resulting in the predominant production of an unstable protein lacking exon 7, known as *SMNΔ7*[5]. Despite this, approximately 10% of functional full-length (FL) SMN protein is still produced by the *SMN2* gene[2]. Consequently, the *SMN2* gene serves as a modifier of disease phenotype, with a higher copy number correlating with milder disease severity[6]. In contrast, mice possess a single copy of the *Smn* gene[2]. Notably, while homozygous deletion of both *SMN* genes has not been observed in humans, the homozygous deletion of the *Smn* gene in mice induces morphological alterations and degenerative changes in embryos post-morula stage, ultimately resulting in death at preimplantation stage[7]. This underscores the pivotal role of the *SMN* gene in early embryonic development[8].

Recent research has unveiled the extensive impact of SMN depletion beyond motor neurons, implicating additional tissues such as the liver and pancreas in both SMA patients and mouse models of SMA[9-12]. Despite major therapeutic advancements focusing on restoring SMN levels, which have notably enhanced both lifespan and quality of life in SMA patients, complete phenotypic rescue remains elusive[4,13,14]. Additionally, existing therapies primarily target postnatal treatment, potentially overlooking crucial developmental changes stemming from SMN depletion. This underscores the likelihood of a broader role for the *SMN* gene in multiple non-neuronal cell types, necessitating further exploration.

Attention has been increasingly drawn to the liver as a critical area of investigation in SMA research. Both clinical studies and preclinical mouse models have unveiled disruptions in fatty acid metabolism, leading to an increased susceptibility among SMA patients to dyslipidemia and liver steatosis[12,15-18]. Given its multifaceted role in regulating numerous biological functions, including the storage and regulation of lipids, carbohydrates, amino acids, and iron, as well as the synthesis of essential growth factors and the clearance of toxic metabolites, any disruptions in liver function may have deleterious effects on other tissues[19].

To explore the role of SMN in the liver, prior studies have utilized a transgenic mouse model featuring the Cre recombinase transgene driven by the α-fetoprotein promoter (*Alfp-Cre*). This approach led to near-total depletion of SMN protein specifically in the liver, resulting in severe impairment of liver development and late embryonic lethality[8]. In our study, to better represent the level of SMN depletion in the liver observed in SMA and elucidate the intricate interplay between SMN deficiency in the liver and its systemic impact in SMA-like pathology, we utilized a mouse model employing *Alb-Cre*, where the albumin promoter drives expression of Cre recombinase in a liver-specific manner. This model also harbors one Smn^{2B} allele and one *Smn* exon 7 allele flanked by loxP sites (F7). The Smn^{2B} allele contains a 3-base pair substitution in

the mouse *Smn* gene, resulting in aberrant splicing of exon 7[20,21]. Consequently, this genetic approach results in the production of approximately 30% full-length functional SMN protein production in the liver.

Our findings reveal that our novel liver-specific SMN depleted (herein referred to as $Alb^{Cre/+};Smn^{2B/F7}$) mouse model induces mild liver steatosis and disrupts pancreatic function at postnatal day 19 (P19), characterized by decreased insulin-positive and increased glucagon-positive cells, alongside reduced blood glucose levels. However, both liver and pancreatic defects were rescued by P60. Remarkably, this mouse model does not exhibit an overt SMA phenotype, demonstrating normal lifespan and motor function. Nevertheless, our data suggests an intricate relationship between hepatic function and pancreatic abnormalities in SMA, thereby enhancing our comprehension of the disease's pathophysiology.

2. Results

2.1 Generation of liver-specific SMN-depleted mice

To elucidate the impact of liver-specific SMN depletion on both CNS and peripheral tissue pathology, we utilized mice expressing Cre recombinase under the control of the mouse albumin promoter, referred to as Alb^{Cre}. This strain is commonly employed for liver-specific gene knockout using the Cre/loxP system[22]. We generated the $Smn^{2B/F7}$ genotype by crossing $Smn^{F7/F7}$ with $Smn^{2B/2B}$ mice (Fig. 1A). The $Smn^{2B/F7}$ genotype carries one allele harboring a three nucleotide switch in the exon splicing enhancer within exon 7 of the mouse *Smn* gene (known as Smn^{2B} allele), mimicking the *SMN2* gene in humans[21], while the other allele features exon 7 flanked by l*oxP* sites[23]. Additionally, crosses between Alb^{Cre} and $Smn^{F7/F7}$ yielded $Alb^{Cre/+};Smn^{F7/+}$ offspring.

The liver-specific mouse line was subsequentially established through further genetic crosses between $Alb^{Cre/+};Smn^{F7/+}$ and $Smn^{2B/F7}$, resulting in various genotypes, including $+/+;Smn^{2B/F7}$ (Fig. 1B), and $Alb^{Cre/+};Smn^{2B/F7}$ (Fig. 1C). As $+/+;Smn^{2B/F7}$ mice lack Cre recombinase, they were used as heterozygous controls. In contrast, recombination occurs in $Alb^{Cre/+};Smn^{2B/F7}$ animals resulting in the specific deletion of one allele of exon 7 in the liver, while the *Smn*2B allele remains unaffected.

$Smn^{2B/-}$ mice, the severe mouse model of SMA, express approximately 15% residual full-length SMN (FLSMN) compared to $Smn^{2B/+}$ heterozygous mice[24]. Therefore, both genotypes were included in this study as additional controls. Tissues were collected at postnatal day 19 (P19), corresponding to the symptomatic phase of the $Smn^{2B/-}$ mouse model. At this stage, $Smn^{2B/-}$ mice show increased liver steatosis and metabolic defects, ultimately culminating in multiple system defects and mortality, typically occurring around P25[25]. In contrast, $Smn^{2B/+}$ mice have slightly reduced levels of FLSMN and no overt phenotypical changes compared to wild-type mice[10].

We first assessed SMN protein levels in the liver and across CNS and peripheral tissues. Our findings confirmed a reduction in SMN protein levels across various tissues in $Smn^{2B/-}$ mice (Fig. 1D-H). However, in $Alb^{Cre/+};Smn^{2B/F7}$, there was a ~70% decrease in FLSMN protein expression in the liver (Fig. 1D, D') compared to littermate control counterparts ($+/+;Smn^{2B/F7}$). Conversely, SMN protein levels in the brain (Fig. 1E, E'), muscle (Fig. 1F, F'), spinal cord (Fig.

1G, G') and pancreas (Fig. 1H, H') remained unaltered, indicating that deletion of *Smn* exon 7 was restricted to the liver in *Alb*$^{Cre/+}$;*Smn*$^{2B/F7}$mice. We validated these findings by assessing Cre expression in liver, pancreas, and spinal cord tissues (Supp. Fig. 1A). Cre expression was exclusively observed in the liver, where it exhibited variable expression across hepatocytes, with some cells showing detectable expression while others showed no expression, confirming the stochastic nature of Cre activity in our model. No Cre signal was detected in either the pancreas or spinal cord tissues.

2.2 Alb$^{Cre/+}$*;Smn*$^{2B/F7}$ *mice show mild yet important liver steatosis*

We previously showed that *Smn*$^{2B/-}$ mice exhibit defects in fatty acid metabolism and lipid accumulation in the liver[12,16-18]. Additionally, SMA patients face an elevated risk of dyslipidemia and steatosis[12]. Hence, we explored whether the intrinsic decrease in SMN levels restricted to the liver would lead to increased lipid accumulation. Histology from *Alb*$^{Cre/+}$;*Smn*$^{2B/F7}$ mice (Fig. 2A) qualitatively indicates some level of hepatic microvesicular steatosis and lipid accumulation. However, there was a noticeable variation in cell morphology and Oil Red-O retention among hepatocytes, suggesting incomplete recombination.

Consistent with the histological findings, *Alb*$^{Cre/+}$;*Smn*$^{2B/F7}$ mice showed variable triglycerides levels (n1=45.95, n2=10.10; n3=75.72; n4=21.91 μg/mg, mean±SEM 38.44±14.48) (Fig. 2B), and yet higher than those observed in +/+;*Smn*$^{2B/F7}$ controls (n1=2.60, n2=0.15; n3=0.66; n4=1.44 μg/mg, mean±SEM 1.213±0.5332), although this difference did not reach statistical significance (p=0.0824). As expected, *Smn*$^{2B/-}$ controls exhibited increased lipid accumulation and triglyceride levels. Taken together, the data suggest an intrinsic role of SMN in regulating fat liver metabolism.

We next sought to identify whether *Alb*$^{Cre/+}$;*Smn*$^{2B/F7}$ mice display disturbed liver homeostatic function. Specifically, we evaluated parameters associated with iron metabolism (Fig. 2C,C',D,D'), endoplasmic reticulum stress (Fig. 2E,E'), and insulin-like growth factor-1 (IGF-1) (Fig. 2F) levels, all of which have previously been identified as altered in *Smn*$^{2B/-}$ mice[18] and were further confirmed in our study. Our analysis revealed no significant differences in the protein levels of heme oxygenase, transferrin, P62, and IGF-1 between the *Alb*$^{Cre/+}$;*Smn*$^{2B/F7}$ and +/+;*Smn*$^{2B/F7}$ control groups. These findings suggest that liver-specific SMN depletion may not play a significant role in these pathways or that the mosaic nature of Cre-mediated excision led to a subtle effect that is difficult to detect.

2.3 Liver-specific SMN-depleted mice display pancreatic defects

We have demonstrated pancreatic and glucose abnormalities in the *Smn*$^{2B/-}$ mouse model of SMA and type I SMA patients[11,26]. Therefore, we conducted immunohistochemistry to investigate the cellular profile of the pancreas, aiming to ascertain whether the targeted depletion of SMN in the liver contributes to pancreatic dysfunction. Surprisingly, double-labeling of insulin-producing β cells and glucagon-producing α cells revealed a significant decrease in the proportion of β cells and a notable increase in α cells in the pancreas of *Alb*$^{Cre/+}$;*Smn*$^{2B/F7}$ mice compared to +/+;*Smn*$^{2B/F7}$ and *Smn*$^{2B/+}$ heterozygous controls (Fig. 3A,B,F). This loss of β cells and rise in α

cells could suggest a functional impairment in glucose metabolism. Consequently, we evaluated non-fasting glucose levels in these mice (Fig. 3C), revealing reduced blood glucose levels in *Alb*$^{Cre/+}$;*Smn*$^{2B/F7}$ mice relative to +/+;*Smn*$^{2B/F7}$ and *Smn*$^{2B/+}$. However, blood glucose levels remained higher than those observed in *Smn*$^{2B/-}$ mice. Overall, these findings indicate imbalances in α and β cell fate within pancreatic islets in *Alb*$^{Cre/+}$;*Smn*$^{2B/F7}$ mice, resembling those observed in *Smn*$^{2B/-}$ mice.

In previous work, we demonstrated that *Smn*$^{2B/-}$ mice exhibit a normoinsulinemic plasma state, despite persistent hypoglycemia and reduced C-peptide levels at P19[18], findings that were recapitulated in this study (Fig. 3C-E). Similarly, *Alb*$^{Cre/+}$;*Smn*$^{2B/F7}$ mice showed no significant changes in plasma insulin levels. However, surprisingly, C-peptide levels in these mice were comparable to those observed in +/+;*Smn*$^{2B/F7}$ and *Smn*$^{2B/+}$ heterozygous controls (Fig. 3E). Additionally, we observed a marked increase in plasma glucagon levels (Fig. 3G) as well as elevated glucagon-like peptide (GLP-1) levels, a product of proglucagon processing (Fig. 3H), reaching levels similar to those seen in *Smn*$^{2B/-}$ mice. These changes likely reflect an increase in pancreatic α-cell numbers, though they were not accompanied by dysregulation of plasma pancreatic polypeptide (PP, Fig. 3I) or amylin (Fig. 3J) hormone production. Furthermore, the maintenance of SMN protein expression at levels comparable to those of heterozygous controls in the pancreas (Fig. 1H,H') suggests that selective SMN depletion in the liver may be implicated in the dysfunction of the pancreas-liver axis.

2.4 Motor neurons, neuromuscular junction (NMJ) or motor fibers are unaffected in liver-specific SMN-depleted mice

The hallmark features of SMA include the degeneration of lower spinal motor neurons, neuromuscular junction (NMJ) pathology, and muscle atrophy[10,25,27-33]. While the exact mechanisms linking these changes in the motor unit to the clinical manifestations of SMA remain unclear, diminished levels of SMN protein are recognized as a pivotal factor[1,2,25,33-35]. Thus, we investigated the impact of liver-specific SMN depletion on these SMA-like features. Our findings show no significant differences in motor neuron cell body counts (Fig. 4A,B), neurofilament accumulation at NMJs (Fig. 5A,B), NMJ endplate occupancy (Fig. 5A,C), muscle fiber size (Fig. 6A,B), or muscle fiber frequency distribution (Fig. 6C) among *Alb*$^{Cre/+}$;*Smn*$^{2B/F7}$ and +/+;*Smn*$^{2B/F7}$ and *Smn*$^{2B/+}$ heterozygous controls. However, as anticipated, *Smn*$^{2B/-}$ mice exhibited motor neuron loss, NMJ defects, and muscle atrophy.

2.5 Liver-specific SMN-depleted mice show transitory liver and pancreatic pathology

We next assessed *Alb*$^{Cre/+}$;*Smn*$^{2B/F7}$ mice at P60 to determine whether liver and pancreatic dysfunction persisted or improved during early adulthood. Histological analysis revealed no significant changes in hepatocyte morphology (as assessed by H&E staining) or lipid accumulation (evaluated with Oil Red O staining) in *Alb*$^{Cre/+}$;*Smn*$^{2B/F7}$ mice at this time point (Fig. 7A). These findings suggest that proliferating non-recombined cells may help restore liver homeostasis over time. Notably, the expression of Cre recombinase was also observed at P60 (Supp. Fig. 1B), indicating stable Cre activity across postnatal development.

Further examination of pancreatic tissue at P60 showed no significant differences in insulin-producing β cells or glucagon-producing α cells in *Alb*$^{Cre/+}$;*Smn*$^{2B/F7}$ mice compared to +/+;*Smn*$^{2B/F7}$ and *Smn*$^{2B/+}$ heterozygous controls (Fig. 7B, C, G). Additionally, non-fasting plasma glucose, insulin, and C-peptide levels in *Alb*$^{Cre/+}$;*Smn*$^{2B/F7}$ mice were similar to those in the control groups (Fig. 7D-F). Moreover, no significant changes in plasma glucagon (Fig. 7H), GLP-1 (Fig. 7I), pancreatic polypeptide (Fig. 7J), or amylin hormone production were observed. Collectively, these results suggest that the liver and pancreatic defects observed in *Alb*$^{Cre/+}$;*Smn*$^{2B/F7}$ mice may be transient, potentially linked to the stochastic nature of Cre recombinase activity in our model and the highly proliferative properties of hepatocytes. In addition, these findings suggest that liver-specific SMN may play a role in regulating pancreatic function, a mechanism that warrants further investigation.

2.6 Liver-specific SMN depletion does not affect major adipocyte and gastrointestinal hormones

Gastrointestinal (GI) hormones play a key role in regulating hepatic lipid metabolism and pancreatic function[36]. Thus, to assess whether adipocytes and GI hormones contribute to liver and pancreatic dysfunction in liver-specific SMN-depleted mice, we measured plasma levels of major adipocyte hormones (leptin and resistin) and GI hormones (ghrelin, gastric inhibitory polypeptide (GIP), peptide YY (PYY) and secretin) at P19 and P60[36,37]. Our data revealed no significant changes in adipocyte hormones at either time point (Fig. 8A-B, G-H) across all genotypes. Moreover, few alterations in GI hormones (Fig. 8C-F, I-L) were observed exclusively in *Smn*$^{2B/-}$ mice at P19, including a marked reduction of ghrelin (Fig. 8C) – a hormone involved in glucose homeostasis in pancreatic islet and liver[38] – and secretin (Fig. 8F), which regulates secretory activity in organs such as the liver and pancreas[39]. Notably, no such changes were observed in *Alb*$^{Cre/+}$;*Smn*$^{2B/F}$ at any time point. Altogether, these results suggest that the pancreatic and liver changes at P19 are likely independent of major adipocyte and GI hormone alterations, pointing to a more direct disruption of the liver-pancreas axis in liver-specific SMN-depleted mice.

2.7 Liver-specific SMN-depleted mice have normal survival rates and motor function

We also conducted a comprehensive assessment of survival, weight, and motor function in *Alb*$^{Cre/+}$;*Smn*$^{2B/F7}$ and +/+;*Smn*$^{2B/F7}$ mice up to postnatal day 60 (Fig. 9A). While the *Smn*$^{2B/-}$ mice typically have a mean survival of 25 days[25], both *Alb*$^{Cre/+}$;*Smn*$^{2B/F7}$ and +/+;*Smn*$^{2B/F7}$ mice in our study survived up to 60 days (Fig. 9B), after which they were euthanized for tissue collection. Moreover, throughout the observation period, mice from both groups exhibited similar weight gain trends (Fig. 9C). When weight gain at P60 was normalized to the basal weight at P7, no statistically significant differences were observed (Fig. 9D).

To further evaluate motor function at different stages, we implemented several age-specific behavioral tests commonly used to assess motor function[40] (Fig. 9E-G). We previously showed *Smn*$^{2B/-}$ mice have reduced motor function scores, as seen through increased time to right, prolonged balancing time and diminished muscle strength[26]. Here, we found no alterations in *Alb*$^{Cre/+}$;*Smn*$^{2B/F7}$ compared to +/+;*Smn*$^{2B/F7}$ mice in time to right, as assessed by the righting reflex (Fig. 9E), nor in distal muscle strength measured through the inverted mesh grip test (Fig.

9F), or motor balance and coordination evaluated by the pen test (Fig. 9G). Overall, these findings collectively demonstrate that liver-specific SMN depletion does not impact survival, weight gain, or motor function.

3. Discussion

The liver is pivotal in regulating numerous biological functions in the body. These encompass, among others, the storage and balance of lipids, carbohydrates, and iron, as well as the synthesis of vital growth factors and the clearance of non-essential or harmful metabolites[19]. Given its multifaceted role, any alterations in liver function can potentially have cascading effects on other organs within the body. Hence, aside from elucidating the impact of liver-specific SMN depletion on hepatic function, it is imperative to explore its effects on other tissues, as alterations in these tissues have been documented in various mouse models of SMA[11,18,34,41].

Previous work on conditional knockout of *Smn* in the livers of mice resulted in severe impairment of liver development characterized by iron overload and subsequent liver atrophy, ultimately leading to late embryonic lethality[8]. In our study, we generated a novel mouse model where instead of a complete knockout of *Smn* in the liver, we created a scenario where SMN protein was depleted to 30% of full-length SMN production specifically within the liver, while SMN protein levels in other tissues remain comparable to those of heterozygous controls. Notably, this mouse line did not exhibit any signs of developmental delays, liver atrophy, or reduced lifespan. Nonetheless, within 19 days after birth, $Alb^{Cre/+};Smn^{2B/F7}$ mice showed a mild yet rapid onset of fatty liver disease and trends towards an increase in lipid levels when maintained on a normal chow diet, underscoring the importance of SMN in lipid metabolism. Interestingly, these changes were transient, as by P60, liver-specific SMN-depleted mice displayed no lipid accumulation or hepatocyte morphological changes, likely due to the compensatory proliferation of non-recombined cells.

A recent study found that 75% of pediatric and adult SMA patients showed ultrasonic evidence of mild to moderate hepatic steatosis, independent of disease severity or SMA subtype[42]. In an *in vitro* model using SMA patient-derived induced pluripotent stem cell-derived hepatocyte-like cells (iHeps), a 10-fold increase in lipid accumulation was observed, correlating with reduced SMN protein expression. Proteomic and transcriptomic analyses revealed dysregulation in mitochondrial and lipid metabolism pathways, including downregulation of key genes involved in oxidative phosphorylation and fatty acid oxidation, alongside increased lipid biosynthesis. Notably, repletion of SMN in SMA iHeps restored metabolic and hepatic functions, rescuing steatosis and mitochondrial defects[42]. Excitingly, our current work further supports these findings, demonstrating that treatment with an adeno-associated viral vector carrying a liver-specific albumin promoter in $Smn^{2B/-}$ mice resulted in partial restoration of liver SMN levels, improving survival, alleviating liver pathology, and restoring muscle size and pancreatic cell balance[43]. Additionally, a recent study found that 60.8% of adult SMA type 3 patients (23 patients) exhibited at least one lipid abnormality[44], further supporting the hypothesis that hepatocyte-specific SMN deficiency contributes to liver pathology.

Mild liver steatosis may be accompanied by disruptions in crucial liver function markers, notably those implicated in iron metabolism, autophagy, and growth factor regulation, such as IGF-1[18].

Accordingly, we initially investigated the expression of HO-1, an enzyme responsible for heme degradation into iron, carbon monoxide, and biliverdin; and transferrin, a liver-synthesized glycoprotein involved in iron transport across tissues (reviewed in[45]). Prior studies have documented alterations in these proteins in *Smn*$^{2B/-}$ mouse livers[18]. While our current analysis did not reveal significant differences in *Alb*$^{Cre/+}$;*Smn*$^{2B/F7}$ mice, the observed upward trend in transferrin and HO levels suggests ongoing changes in iron metabolism, which may not be fully manifested at P19. In addition, incomplete Cre-mediated excision of *Smn*^{F7} allele may be hindering a comprehensive understanding of SMN's role in liver function.

Furthermore, no alterations were observed for P62 levels, a multifunctional scaffold protein implicated in autophagy, formation of hepatic inclusion bodies, and hepatocyte cell death (reviewed in[46]) despite its increased presence in mouse models of SMA[18]. Similarly, there were no changes detected in IGF-1 protein levels, whose deficiency has been linked to liver pathology and non-alcoholic fatty liver disease (NAFLD)[47,48], and its decrease is evident in *Smn*$^{2B/-}$ mice[18]. NAFLD involves the accumulation of fatty acids in more than 5% of liver cells, occurring in the absence of alcohol consumption. This condition presents with varying degrees of severity, with simple steatosis being the most common manifestation. Simple steatosis is characterized by the accumulation of fat in the liver with minimal impact on liver function[49,50]. Consequently, our model holds promise as a valuable resource for investigating microvesicular steatohepatitis and NAFLD during the early postnatal period. Additionally, unlike the well-studied *Smn*$^{2B/-}$ model of SMA, this liver-specific SMN depletion enables the study of hepatic SMN function without the confounding effects of systemic SMN depletion or the severe phenotype observed in the *Smn*$^{2B/-}$ mice.

Previously, our research unveiled metabolic abnormalities in SMA-like mice, including glucose intolerance, insulin hypersensitivity, and hyperglucagonemia, accompanied by changes in pancreatic islet composition characterized by an increase in glucagon-producing α-cells at the expense of insulin-producing β-cells[11]. Histopathological examination of pancreatic tissue from infants and children with SMA type I corroborated these findings, revealing a predominant presence of glucagon-producing α-cells within pancreatic islets[11]. Furthermore, one-year-old *Smn*$^{+/-}$mice producing approximately 50% of SMN protein, when exposed to a high-fat diet, exhibited dysregulation in the proportion of glucagon-producing α-cells within pancreatic islets and heightened hepatic insulin and glucagon sensitivity[9].

Here, we uncovered a novel intrinsic role of liver-specific SMN in pancreatic function, distinct from IGF-1 signaling, pancreatic SMN levels (which remained stable), or canonical SMA pathology. Although the precise role of SMN in the liver-pancreas axis remains unclear, we speculate that altered amino acid metabolism may contribute to the disrupted communication between these two organs. The liver plays a central role in amino acid metabolism, and disturbances in this process can affect the liver-α cell axis, a well-documented feedback loop in which circulating amino acids stimulate glucagon secretion, which in turn regulates hepatic amino acid uptake and metabolism[51]. In the context of metabolic diseases such as NAFLD and SMA, liver dysfunction, including impaired lipid metabolism, may disrupt this axis, leading to abnormal glucagon secretion[51,52]. It is possible that dysregulated amino acid pathways may directly influence this feedback loop.

Further evidence for this hypothesis comes from a recent study in individuals with type 2 diabetes (T2D) and NAFLD, which found hyperglucagonaemia and altered amino acid profiles. In T2D-NAFLD patients, plasma glucagon levels were significantly higher than in individuals without NAFLD, with a positive correlation between plasma glucagon concentrations and liver fat content. This study also showed increased plasma levels of isoleucine and glutamate, and decreased levels of glycine and serine in individuals with NAFLD[53]. These findings suggest that metabolic dysregulation in the liver, including alterations in amino acid metabolism, may exacerbate glucagon secretion. Interestingly, such changes in amino acid metabolism are consistent with clinical observations in SMA patients, where an "amino acid diet" — low in fats and rich in specific amino acids — has been shown to provide some clinical benefit[54]. Given this, it is plausible that impaired liver metabolism in SMN-depleted mice alters the liver-α cell axis, leading to dysregulated glucagon and GLP-1 secretion. While this proposed link between liver steatosis, amino acid metabolism, and pancreatic dysfunction is speculative, we are actively investigating the mechanisms underlying this liver-pancreas interplay in mouse models of SMA.

In addition, while the hallmark pathological features of SMA include motor neuron loss, NMJ pathology, muscle atrophy, and consequent motor function alterations, these were not evident in the $Alb^{Cre/+}$;$Smn^{2B/F7}$ mouse model at P19. However, given that glucose metabolism defects are observed in various neurodegenerative and neuromuscular disorders, subsequent work is required to clarify the impact of liver-specific SMN depletion on pancreatic function. Although hepatic and pancreatic abnormalities likely occur independently of disease onset, given that SMN depletion in motor neurons and muscle alone is sufficient to induce a SMA-like phenotype[23,55,56], the potential influence of these anomalies on SMA progression warrants careful consideration.

Overall, our findings suggest that alterations in SMN production solely within the liver may suffice to induce pathological hepatic and pancreatic function, shedding light on a novel role of SMN in liver physiology.

4. **Material and Methods**

4.1 Mouse models

The Smn^{2B} mouse, which harbors the Smn^{2B} mutation resulting from the substitution of three nucleotides within the exon splicing enhancer of exon 7, was developed and maintained on a C57BL/6 background in our laboratory[10,24]. The FVB.129(B6)-$Smn1^{tm1Jme}$ ($Smn^{F7/F7}$) and B6.Cg-$Speer6\text{-}ps1^{Tg(Alb\text{-}Cre)21Mgn}$/J ($Alb^{Cre}$) mice were acquired from The Jackson Laboratory. Liver-specific SMN-depleted mice were obtained through successive crosses between $Alb^{Cre/+}$;$Smn^{F7/+}$ and $Smn^{2B/F7}$ mice (see Fig. 1). Line validation was conducted via genotyping of DNA extracted from mouse ear biopsies using PCR (see Table 1 for list of primers used). Both male and female mice were included in the studies. All mice were bred and housed in the University of Ottawa Animal Facility under protocol OHRI-3343, adhering to guidelines established by the Canadian Council on Animal Care. Additionally, we employed $Smn^{2B/-}$ mice (a severe SMA mouse model) and asymptomatic heterozygous $Smn^{2B/+}$ mice as controls in our experiments.

Table 1. List of primers used for genotyping

NAME	SEQUENCE (5'-3')
Alb-Cre	TGCAAACATCACATGCACAC
	TTGGCCCCTTACCATAACTG
	GAAGCAGAAGCTTAGGAAGATGG
SmnF7	AGAAGGAAAGTGCTCACATACAAATT
	TGTCTATAATCCTCATGCTATGGAG
Smn2B	GGTTTCAGACAAAATAAAAAAGAATTTAAG
	TTTGGCAGACTTTAGCAGGGC

4.2 Tissue harvesting and processing

Following euthanasia, liver, and *tibialis anterior* (TA) muscles underwent fixation in a 1:10 dilution of buffered formalin for 48 h at 4°C, followed by transfer to 70% ethanol at the same temperature until processing. The pancreas was fixed in 4% paraformaldehyde (PFA) for 48 h at 4°C, then similarly moved to 70% ethanol for processing. For the lumbar spinal cord (SC) and liver (for Oil Red-O staining), fixation was performed overnight at 4°C in 4% PFA, followed by immersion in 30% sucrose in PBS. Subsequently, the liver and spinal cord were flash-frozen in optimal cutting temperature (OCT) embedding medium. Cryosections of the lumbar spinal cord were cut at a thickness of 16 μm, while liver sections were cut at 10 μm and stored at -80°C until immunohistochemical analysis. Cre immunostaining of cryosectioned liver and spinal cord was performed as described in section 4.4.1, with the exception that the antigen retrieval step was not performed.

The abdominal musculature was dissected and fixed in 4% PFA for 15 min at room temperature, followed by 3 washes in 1X PBS, after which the transversus abdominis (TVA) muscle was dissected from the abdominal musculature. TA, liver, and pancreas samples were handled at the University of Ottawa Department of Pathology and Laboratory Medicine. Paraffin blocks containing tissues were sectioned at 4 μm thickness using a microtome. Sections of TA and liver were stained with hematoxylin and eosin (H&E) using an XL CV5030 autostainer from Leica. Liver cryosections were stained with Oil Red-O and counterstained with hematoxylin using established protocols. Images of H&E and Oil Red-O-stained samples were scanned with a MIRAX MIDI digital slide scanner manufactured by Zeiss. Image acquisition was performed using Panoramic Viewer 1.15.4 software.

4.3 Immunoblotting

Total protein was extracted by homogenizing flash-frozen samples of spinal cord, brain, liver, pancreas and hindlimb muscles using RIPA lysis buffer (Cell Signaling), supplemented with phenylmethylsulfonyl fluoride (PMSF, Cell Signaling). The concentrations of the extracted proteins were determined using the Pierce BCA Protein Assay kit (ThermoFisher).

For liver, brain, and spinal cord tissues, 20 μg of protein per sample were separated by 10% sodium dodecyl sulfate polyacrylamide gel electrophoresis (SDS-PAGE), while 30 μg were used for pancreas and muscle samples. Following electrophoresis, the proteins were transferred onto a PVDF membrane (Immobilon-P, Millipore) and blocked for 30 min at room temperature using

intercept blocking buffer (LI-COR). Subsequently, the membranes were incubated overnight at 4°C with primary antibodies.

After incubation, the membranes were rinsed with tris-buffered saline containing 0.1% Tween-20 (TBS-T) and then incubated for 1 h at room temperature with IRDye 680R or 800CW (LI-COR) secondary antibody. Fluorescent signals were detected using the Odyssey Infrared Imaging System (LI-COR). Total raw values were normalized to α-tubulin (housekeeping protein) obtained from the same blot.

4.4 Immunohistochemistry

4.4.1 Pancreas

Pancreatic sections underwent deparaffinization using three washes of Histo-Clear (National Diagnostics, Atlanta, GA) for 5 min each, followed by two washes of a 50/50 mixture of absolute ethanol and Histo-Clear for 3 min each. Subsequently, the slides were gradually rehydrated in two washes of 100% (v/v) ethanol (3 min each), followed by one wash of 95% (v/v), 70% (v/v), 50% (v/v), and 0% (v/v) ethanol for 3 min each. The slides were then incubated in 0.5% Triton-X-100 (Millipore Sigma, Burlington, MA) in PBS for 5 min, followed by three washes with PBS. Afterward, the slides were blocked in a solution containing 20% goat serum and 0.3% Triton-X-100 in TBS for 2 h.

Primary antibodies targeting insulin, glucagon or Cre (Table 2) were applied to the slides in a solution containing 2% goat serum and 0.3% Triton-X-100 in TBS overnight at 4°C. The slides were then washed three times with PBS and subsequently incubated with secondary antibodies in a solution containing 2% goat serum and 0.3% Triton-X-100 for 1 h. Following this, the solution was removed, and DAPI (1:1,000) in PBS was added for 5 min at room temperature. The slides were washed three times with PBS and mounted in Fluoromount-G™ Mounting Medium (Invitrogen).

Images were taken using an Axio Imager M2 microscope (Zeiss) and captured with a 40X objective. The number of glucagon and insulin positive cells per islet was counted for each mouse.

4.4.2 Motor neurons

Lumbar spinal cord sections were prepared for choline acetyltransferase (ChAT) staining of motor neurons. The slides were air-dried at room temperature for 30 min and then rinsed in TBS-T for 5 min. Samples were permeabilized in 0.3% Triton X-100 in PBS for 30 min, followed by blocking in 1x Power Block (BioGenex, Fremont, CA) for 20 min at room temperature. Subsequently, the samples were incubated with a goat anti-ChAT (details in Table 2) antibody at a dilution of 1:100 in 1% BSA and 0.3% Triton X-100 in PBS for 3 nights at 4°C.

After the initial antibody incubation, slides were washed twice for 10 min with TBS-T at room temperature. Following the washes, samples were then incubated with Alexa Fluor 555 donkey anti-goat IgG at a dilution of 1:200 in 10% donkey serum and 0.3% Triton X-100 in PBS for 2 h

at room temperature in a humid chamber. Nuclei were counterstained with 4',6-diamidino-2-phenylindole (DAPI) at a dilution of 1:1000 in PBS for 5 min.

Finally, the slides were rinsed 3X for 10 min with TBS-T and mounted with Fluoromount-G™ Mounting Medium (Invitrogen). Spinal cord sections were examined under fluorescence using an Axio Imager M2 microscope (Zeiss) and imaged at 20X magnification for quantification, and at 63x for representative pictures. The number of ChAT-positive motor neurons with a diameter of ≥20 μm per ventral horn was recorded for 7-10 different sections per animal, each separated by at least 100 μm to prevent re-counting of the same motor neuron. An average number of motor neuron cell bodies per section was determined.

4.4.3 Neuromuscular Junction (NMJ)

To evaluate neuromuscular innervation, we performed immunohistochemistry using established protocols[26]. After euthanasia, the TVA muscles were promptly dissected and fixed in 4% paraformaldehyde (Electron Microscopy Science) in PBS for 15 min. Post-synaptic acetylcholine receptors (AChRs) were labeled for 10 min with alpha-bungarotoxin (aBTX) conjugated to Alexa Fluor 488. Subsequently, the muscles were blocked in 4% bovine serum albumin (BSA) and 1% Triton-X-100 in PBS for 30 min.

Following blocking, the muscles underwent overnight incubation with primary antibodies for neurofilament and synaptic vesicle protein 2 (refer to Table 2). Visualization of the labeled structures was achieved using DyLight-conjugated secondary antibodies. The muscles were then whole-mounted in Dako Fluorescent mounting media and imaged with a 20x objective on a Zeiss Axio Imager M1 microscope.

A minimum of three fields of view (FOV) were quantified per muscle. For each FOV, the percentage of fully occupied endplates was noted. Fully occupied endplates were defined as motor endplates completely covered by the presynaptic terminal labeled with synaptic vesicle protein 2 (SV2) and neurofilament (NF).

Table 2. List of antibodies used.

Application	***Antibody***	***Species***	***Dilution***	***Company (Catalog #)***
Western Blot	SMN	Mouse	1:2 500	BD Transduction (610647)
Western Blot	Alpha-tubulin	Rabbit	1:10 000	Abcam (ab4074)
Western Blot	Alpha-tubulin	Mouse	1:10 000	Sigma-Aldrich (CP06)
Western Blot	Heme oxygenase-1 (HO)	Rabbit	1:10 000	Abcam (ab68477)
Western Blot	P62	Mouse	1:1 000	Abcam (ab56416)

Western Blot	Transferrin	Rabbit	1:1 000	Abcam (ab82411)
Western Blot	Goat anti-mouse IR Dye 800 CW		1:5 000	LI-COR (925-32210)
Western Blot	Goat anti-mouse IR Dye 680 R		1:5 000	LI-COR (926-68070)
Western Blot	Goat anti-rabbit IR Dye 800 CW		1:5 000	LI-COR (925-32211)
Western Blot	Goat anti-rabbit IR Dye 680 R		1:5 000	LI-COR (926-68071)
IHC	ChAT	Goat	1:100	Millipore (AB144P)
IHC	Donkey anti-goat Alexa Fluor 555		1:200	Invitrogen (A21432)
IHC	TRITC conjugated bungarotoxin	N/A	1:1 000	Invitrogen (T1175)
IHC	Neurofilament (NF-M)	Mouse	1:100	(Developmental Studies Hybridoma Bank, P12839)
IHC	Synaptic vesicle glycoprotein 2A (SV2A)	Mouse	1:250	(Developmental Studies Hybridoma Bank, Q7L0J3)
IHC	Goat anti-mouse Alexa Fluor 488		1:250	Invitrogen (A11001)
IHC	Glucagon	Mouse	1:200	Abcam (ab10988)
IHC (Parafin) IHC (Frozen)	Cre Recombinase (D7L7L)	Rabbit	1:500 1:200	Cell Signaling (15036)
IHC	Insulin	Rabbit	1:50	Abcam (ab181547)
IHC	Goat anti-mouse Alexa Fluor 555		1:500	Invitrogen (A21422)
IHC	Goat anti-rabbit Alexa Fluor 488		1:500	Invitrogen (A11034)

4.5 Muscle fiber analysis

Muscle fiber analysis was performed using ImageJ software (version 2.9.0/1.53t). A total of one hundred fibers were evaluated per animal, covering various regions of the muscle section to ensure good representation. The area of each fiber was measured in square micrometers (μm^2) to compute both the average and distribution of fiber sizes for each animal.

4.6 Glucose levels

Non-fasting blood glucose concentrations were assessed using a OneTouch Ultra2 Blood Glucose Test Strips (LifeScan Europe GmbH, Zug, Switzerland) immediately following blood collection. Approximately 2 µL of blood was applied to the test strip for glucose concentration measurement.

4.7 ELISA for Insulin-like Growth Factor I (IGF-1)

The concentration of IGF-1 in the liver was quantified using the Mouse/Rat IGF-I/IGF1 Quantikine ELISA Kit (MG100, R&D Systems, Inc., Minneapolis, MN, USA). Liver protein lysates were diluted at a ratio of 1:6 in calibrator diluent and the assay was performed following the manufacturer's instructions.

4.8 Triglycerides quantification

Liver tissues from P19 mice were promptly dissected and flash frozen. Subsequently, triglyceride analysis was conducted at the Vanderbilt Mouse Metabolic Phenotyping Center, employing established protocols previously utilized by our team[18].

4.9 Mouse metabolic hormone assay

Blood was collected from the mice immediately after decapitation using a Microcuvette CB 300 K2E coated with K2 EDTA (16.444.100) for capillary sampling. All samples were taken randomly without a fasting period. The blood was centrifuged at 5000 g for 5 minutes at room temperature to separate the plasma. For plasma volumes less than 50 µL, genotypes were pooled to achieve a minimum volume of 50 µL as needed. The multiplexing analysis was performed using the Luminex™ 200 system (Luminex, Austin, TX, USA) by Eve Technologies Corp. (Calgary, Alberta). Twelve markers were simultaneously measured in the samples using Eve Technologies' Mouse Metabolic Hormone 12-Plex Discovery Assay® (MilliporeSigma, Burlington, Massachusetts, USA) according to the manufacturer's protocol. The 12-plex consisted of Amylin(active), C-Peptide 2, Ghrelin, GIP(total), GLP-1(active), Glucagon, Insulin, Leptin, PP, PYY, Resistin and Secretin. Assay sensitivities of these markers range from 1.4 – 91.8 pg/mL for the 12-plex. Individual analyte sensitivity values are available in the MilliporeSigma MILLIPLEX® MAP protocol. If analyte levels were too low to be detected and fell outside the dynamic range, they were recorded as 0 in the graphs.

4.10 Motor function, weight, and survival assessments

Motor function, weight, and survival were assessed according to established protocols[40]. Spinal reflexes were evaluated using the righting reflex test, while motor balance and coordination were evaluated with the pen test. Additionally, muscle strength was measured using the inverted mesh grip test (see Fig. 9A). The righting reflex test was conducted from P7 to P13, the inverted mesh grip test from P13 to P25, and the pen test from P19 to P25. Assessments were performed every two days. A maximum duration of 30 sec for the pen test and 60 sec for the inverted mesh grip represented the established threshold. Three consecutive measurements were obtained, and their average was recorded for subsequent analysis. Weight was measured every two days starting at day 7 until day 30, and then weekly until day 60. Animal welfare was monitored throughout the 60-day period during weight measurements.

4.11 Statistical analysis

Survival data were visualized using Kaplan-Meier survival curves, and intergroup differences were evaluated using the Mantel-Cox test. Brown-Forsythe and Welch ANOVA were employed to compare three or more sets of unpaired measurements, given the mosaic-like outcome observed in the $Alb^{Cre/+};Smn^{2B/F7}$ model, where assumptions of equal variances were not tenable. Two-way ANOVA, followed by Šídák's method for multiple comparisons, was utilized to assess the influence of two factors on a response. Pairwise comparisons were performed using a two-tailed Student's t-test. Statistical analyses were conducted using GraphPad Prism V.10.2.1 (GraphPad Prism Software, San Diego, CA), with significance set at $P < 0.05$. Data were presented as mean ± standard error of the mean. Sample sizes (n) are provided in figure legends, indicating the number of biological replicates analyzed, with each data point corresponding to an individual mouse from at least two different litters. Detailed statistical information is outlined in the respective figure legends, where statistical significance is indicated by *, $p < 0.05$; **, $p < 0.01$; ***, $p < 0.001$.

Data sharing

All authors had access to the study data and reviewed and approved the final manuscript. All data associated with this study are available in the main text or supplementary materials. Raw data can be provided upon request.

Acknowledgements

This work was supported by Muscular Dystrophy Association (USA) [grant number 963652 to R.K.]; the Canadian Institutes of Health Research [grant number PJT-186300 to R.K.]; and the University of Ottawa Brain and Mind Institute TRIMS Award to MMAA.

Declaration of interests

The authors disclose no conflicts of interest. The funders mentioned above were not involved in the study design, data collection and analysis, decision to publish, or manuscript preparation.

Author's contributions:

M.M.A.A. conceived and designed the study, with supervision and support from R.K. The methodology was developed by M.M.A.A., Y.D.R., and S.G. Formal analysis was conducted by M.M.A.A. and E.R.S. The investigation was carried out by M.M.A.A. The manuscript was written by M.M.A.A and critically revised by R.K. Funding acquisition was managed by R.K.

References

1 Lefebvre, S. *et al*. Identification and characterization of a spinal muscular atrophy-determining gene. *Cell* **80**, 155-165 (1995).

2 Lefebvre, S. *et al*. Correlation between severity and SMN protein level in spinal muscular atrophy. *Nat Genet* **16**, 265-269 (1997).

3 Crawford, T. O. & Pardo, C. A. The Neurobiology of Childhood Spinal Muscular Atrophy. *Neurobiology of Disease* **3**, 97-110 (1996).

4 Finkel, R. S. *et al.* Treatment of infantile-onset spinal muscular atrophy with nusinersen: a phase 2, open-label, dose-escalation study. *Lancet* **388**, 3017-3026 (2016). https://doi.org:10.1016/S0140-6736(16)31408-8

5 Lorson, C. L., Hahnen, E., Androphy, E. J. & Wirth, B. A single nucleotide in the SMN gene regulates splicing and is responsible for spinal muscular atrophy. *Proc Natl Acad Sci U S A* **96**, 6307-6311 (1999).

6 Feldkotter, M., Schwarzer, V., Wirth, R., Wienker, T. F. & Wirth, B. Quantitative analyses of SMN1 and SMN2 based on real-time lightCycler PCR: fast and highly reliable carrier testing and prediction of severity of spinal muscular atrophy. *Am J Hum Genet* **70**, 358-368 (2002). https://doi.org:10.1086/338627

7 Schrank, B. *et al.* Inactivation of the survival motor neuron gene, a candidate gene for human spinal muscular atrophy, leads to massive cell death in early mouse embryos. *Proc Natl Acad Sci U S A* **94**, 9920-9925 (1997).

8 Vitte, J. M. *et al.* Deletion of murine Smn exon 7 directed to liver leads to severe defect of liver development associated with iron overload. *Am J Pathol* **165**, 1731-1741 (2004). https://doi.org:10.1016/S0002-9440(10)63428-1

9 Bowerman, M. *et al.* Defects in pancreatic development and glucose metabolism in SMN-depleted mice independent of canonical spinal muscular atrophy neuromuscular pathology. *Hum Mol Genet* **23**, 3432-3444 (2014). https://doi.org:10.1093/hmg/ddu052

10 Bowerman, M., Murray, L. M., Beauvais, A., Pinheiro, B. & Kothary, R. A critical smn threshold in mice dictates onset of an intermediate spinal muscular atrophy phenotype associated with a distinct neuromuscular junction pathology. *Neuromuscul Disord* **22**, 263-276 (2012). https://doi.org:S0960-8966(11)01345-9 [pii] 10.1016/j.nmd.2011.09.007

11 Bowerman, M. *et al.* Glucose metabolism and pancreatic defects in spinal muscular atrophy. *Ann Neurol* **72**, 256-268 (2012).

12 Deguise, M. O. *et al.* Abnormal fatty acid metabolism is a core component of spinal muscular atrophy. *Ann Clin Transl Neurol* **6**, 1519-1532 (2019). https://doi.org:10.1002/acn3.50855

13 Chiriboga, C. A. Nusinersen for the treatment of spinal muscular atrophy. *Expert Rev Neurother* **17**, 955-962 (2017). https://doi.org:10.1080/14737175.2017.1364159

14 McMillan, H. J. *et al.* Onasemnogene abeparvovec for the treatment of spinal muscular atrophy. *Expert Opin Biol Ther* **22**, 1075-1090 (2022). https://doi.org:10.1080/14712598.2022.2066471

15 Crawford, T. O., Sladky, J. T., Hurko, O., Besner-Johnston, A. & Kelley, R. I. Abnormal fatty acid metabolism in childhood spinal muscular atrophy. *Ann Neurol* **45**, 337-343 (1999).

16 Deguise, M. O., Chehade, L. & Kothary, R. Metabolic Dysfunction in Spinal Muscular Atrophy. *Int J Mol Sci* **22** (2021). https://doi.org:10.3390/ijms22115913

17 Deguise, M. O., Chehade, L., Tierney, A., Beauvais, A. & Kothary, R. Low fat diets increase survival of a mouse model of spinal muscular atrophy. *Ann Clin Transl Neurol* **6**, 2340-2346 (2019). https://doi.org:10.1002/acn3.50920

18 Deguise, M. O. *et al.* SMN Depleted Mice Offer a Robust and Rapid Onset Model of Nonalcoholic Fatty Liver Disease. *Cell Mol Gastroenterol Hepatol* **12**, 354-377 e353 (2021). https://doi.org:10.1016/j.jcmgh.2021.01.019

19 Trefts, E., Gannon, M. & Wasserman, D. H. The liver. *Curr Biol* **27**, R1147-R1151 (2017). https://doi.org:10.1016/j.cub.2017.09.019

20 DiDonato, C. J. *et al.* Regulation of murine survival motor neuron (Smn) protein levels by modifying Smn exon 7 splicing. *Hum Mol Genet* **10**, 2727-2736. (2001).

21 Hammond, S. M. *et al.* Mouse survival motor neuron alleles that mimic SMN2 splicing and are inducible rescue embryonic lethality early in development but not late. *PLoS One* **5**, e15887 (2010). https://doi.org:10.1371/journal.pone.0015887

22 Postic, C. *et al.* Dual roles for glucokinase in glucose homeostasis as determined by liver and pancreatic beta cell-specific gene knock-outs using Cre recombinase. *J Biol Chem* **274**, 305-315 (1999). https://doi.org:10.1074/jbc.274.1.305

23 Frugier, T. *et al.* Nuclear targeting defect of SMN lacking the C-terminus in a mouse model of spinal muscular atrophy. *Hum Mol Genet* **9**, 849-858 (2000).

24 Eshraghi, M., McFall, E., Gibeault, S. & Kothary, R. Effect of genetic background on the phenotype of the Smn2B/- mouse model of spinal muscular atrophy. *Hum Mol Genet* **25**, 4494-4506 (2016). https://doi.org:10.1093/hmg/ddw278

25 Reilly, A., Yaworski, R., Beauvais, A., Schneider, B. L. & Kothary, R. Long term peripheral AAV9-SMN gene therapy promotes survival in a mouse model of spinal muscular atrophy. *Hum Mol Genet* **33**, 510-519 (2024). https://doi.org:10.1093/hmg/ddad202

26 Reilly, A. *et al.* Central and peripheral delivered AAV9-SMN are both efficient but target different pathomechanisms in a mouse model of spinal muscular atrophy. *Gene Ther* **29**, 544-554 (2022). https://doi.org:10.1038/s41434-022-00338-1

27 Deguise, M. O. *et al.* Differential induction of muscle atrophy pathways in two mouse models of spinal muscular atrophy. *Sci Rep* **6**, 28846 (2016). https://doi.org:10.1038/srep28846

28 Deguise, M. O. *et al.* Motor transmission defects with sex differences in a new mouse model of mild spinal muscular atrophy. *EBioMedicine* **55**, 102750 (2020). https://doi.org:10.1016/j.ebiom.2020.102750

29 Gavrilina, T. O. *et al.* Neuronal SMN expression corrects spinal muscular atrophy in severe SMA mice while muscle-specific SMN expression has no phenotypic effect. *Hum Mol Genet* **17**, 1063-1075 (2008).

30 Murray, L. M., Beauvais, A., Bhanot, K. & Kothary, R. Defects in neuromuscular junction remodelling in the *Smn2B/-* mouse model of spinal muscular atrophy. *Neurobiology of Disease* **49**, 57-67 (2013).

31 Murray, L. M., Beauvais, A., Gibeault, S., Courtney, N. L. & Kothary, R. Transcriptional profiling of differentially vulnerable motor neurons at pre-symptomatic stage in the Smn (2b/-) mouse model of spinal muscular atrophy. *Acta Neuropathol Commun* **3**, 55 (2015). https://doi.org:10.1186/s40478-015-0231-1

32 Shababi, M., Lorson, C. L. & Rudnik-Schoneborn, S. S. Spinal muscular atrophy: a motor neuron disorder or a multi-organ disease? *J Anat* **224**, 15-28 (2014). https://doi.org:10.1111/joa.12083

33 Lorson, C. L., Rindt, H. & Shababi, M. Spinal muscular atrophy: mechanisms and therapeutic strategies. *Hum Mol Genet* **19**, R111-118 (2010). https://doi.org:10.1093/hmg/ddq147

34 Hua, Y. *et al.* Peripheral SMN restoration is essential for long-term rescue of a severe spinal muscular atrophy mouse model. *Nature* **478**, 123-126 (2011). https://doi.org:nature10485 [pii] 10.1038/nature10485

35 Mercuri, E., Sumner, C. J., Muntoni, F., Darras, B. T. & Finkel, R. S. Spinal muscular atrophy. *Nat Rev Dis Primers* **8**, 52 (2022). https://doi.org:10.1038/s41572-022-00380-8

36 Mells, J. E. & Anania, F. A. The role of gastrointestinal hormones in hepatic lipid metabolism. *Semin Liver Dis* **33**, 343-357 (2013). https://doi.org:10.1055/s-0033-1358527

37 Chen, L. *et al.* Inhibition of Secretin/Secretin Receptor Axis Ameliorates NAFLD Phenotypes. *Hepatology* **74**, 1845-1863 (2021). https://doi.org:10.1002/hep.31871

38 Dong, C. X. & Brubaker, P. L. Ghrelin, the proglucagon-derived peptides and peptide YY in nutrient homeostasis. *Nat Rev Gastroenterol Hepatol* **9**, 705-715 (2012). https://doi.org:10.1038/nrgastro.2012.185

39 Afroze, S. *et al.* The physiological roles of secretin and its receptor. *Ann Transl Med* **1**, 29 (2013). https://doi.org:10.3978/j.issn.2305-5839.2012.12.01

40 Chehade, L. *et al.* Suppression of the necroptotic cell death pathways improves survival in Smn (2B/-) mice. *Front Cell Neurosci* **16**, 972029 (2022). https://doi.org:10.3389/fncel.2022.972029

41 Hua, Y. *et al.* Motor neuron cell-nonautonomous rescue of spinal muscular atrophy phenotypes in mild and severe transgenic mouse models. *Genes Dev* **29**, 288-297 (2015). https://doi.org:10.1101/gad.256644.114

42 Leow, D. M. *et al.* Hepatocyte-intrinsic SMN deficiency drives metabolic dysfunction and liver steatosis in spinal muscular atrophy. *J Clin Invest* **134** (2024). https://doi.org:10.1172/JCI173702

43 Sutton, E. R. *et al.* Liver SMN restoration rescues the Smn(2B/-) mouse model of spinal muscular atrophy. *EBioMedicine* **110**, 105444 (2024). https://doi.org:10.1016/j.ebiom.2024.105444

44 Miletic, M. *et al.* Glucose and Lipid Metabolism Disorders in Adults with Spinal Muscular Atrophy Type 3. *Diagnostics* **14** (2024). https://doi.org:10.3390/diagnostics14182078

45 Muckenthaler, M. U., Rivella, S., Hentze, M. W. & Galy, B. A Red Carpet for Iron Metabolism. *Cell* **168**, 344-361 (2017). https://doi.org:10.1016/j.cell.2016.12.034

46 Manley, S., Williams, J. A. & Ding, W. X. Role of p62/SQSTM1 in liver physiology and pathogenesis. *Exp Biol Med* **238**, 525-538 (2013). https://doi.org:10.1177/1535370213489446

47 Hribal, M. L. *et al.* Insulin-like growth factor-I, inflammatory proteins, and fibrosis in subjects with nonalcoholic fatty liver disease. *J Clin Endocrinol Metab* **98**, E304-308 (2013). https://doi.org:10.1210/jc.2012-3290

48 Ichikawa, T. *et al.* Role of growth hormone, insulin-like growth factor 1 and insulin-like growth factor-binding protein 3 in development of non-alcoholic fatty liver disease. *Hepatol Int* **1**, 287-294 (2007). https://doi.org:10.1007/s12072-007-9007-4

49 Loomba, R. & Sanyal, A. J. The global NAFLD epidemic. *Nat Rev Gastroenterol Hepatol* **10**, 686-690 (2013). https://doi.org:10.1038/nrgastro.2013.171

50 Tandra, S. *et al.* Presence and significance of microvesicular steatosis in nonalcoholic fatty liver disease. *J Hepatol* **55**, 654-659 (2011). https://doi.org:10.1016/j.jhep.2010.11.021

51 Richter, M. M. *et al.* The Liver-alpha-Cell Axis in Health and in Disease. *Diabetes* **71**, 1852-1861 (2022). https://doi.org:10.2337/dbi22-0004

52 Deng, Y., Hu, M., Huang, S. & Fu, N. Molecular mechanism and therapeutic significance of essential amino acids in metabolically associated fatty liver disease. *J Nutr Biochem* **126**, 109581 (2024). https://doi.org:10.1016/j.jnutbio.2024.109581

53 Rix, I. *et al.* Hyperglucagonaemia and amino acid alterations in individuals with type 2 diabetes and non-alcoholic fatty liver disease. *Endocr Connect* **13** (2024). https://doi.org:10.1530/EC-23-0161

54 O'Connor, G. *et al.* Open-labelled study to monitor the effect of an amino acid formula on symptom management in children with spinal muscular atrophy type I: The SMAAF pilot study. *Nutr Clin Pract* **38**, 871-880 (2023). https://doi.org:10.1002/ncp.10940

55 Cifuentes-Diaz, C. *et al.* Deletion of murine SMN exon 7 directed to skeletal muscle leads to severe muscular dystrophy. *J Cell Biol* **152**, 1107-1114. (2001).

56 Cifuentes-Diaz, C. *et al.* Neurofilament accumulation at the motor endplate and lack of axonal sprouting in a spinal muscular atrophy mouse model. *Hum Mol Genet* **11**, 1439-1447. (2002).

Figure subtitles

1. **Generation of liver-specific SMN-depleted mice.** A. Schematic representation of the breeding scheme to generate liver-specific SMN depletion. In these mice, the *Smn* gene carries one Smn^{2B} allele that harbors a three-nucleotide switch in exon 7, and one *Smn* allele whose exon 7 is floxed by loxP sites (Smn^{F7}). The *Alb-Cre* transgene has also been crossed into this background to provide liver-specific expression of the Cre recombinase. B. Littermate controls do not harbor Cre recombinase but do carry one Smn^{2B} allele and are thus used as heterozygous controls. C. Upon crossing $Alb^{Cre/+};Smn^{F7/+}$ with $Smn^{2B/F7}$ animals, Cre recombination will induce specific excision of exon 7 in the liver, leading to reduced SMN protein production only in the liver. D-H. Immunoblots were performed to assess SMN protein levels in various tissues from $Smn^{2B/+}$, $Smn^{2B/-}$, +/+;$Smn^{2B/F7}$, and $Alb^{Cre/+};Smn^{2B/F7}$ mice at P19. Membranes were probed for SMN and then reprobed for α-tubulin (loading control). D'-H'. Bar graphs show quantification of SMN protein levels in the liver (D'), brain (E'), muscle (F'), spinal cord (G') and pancreas (H'), normalized to α-tubulin. n□≥□3, mean ± SEM. Statistical significance indicated by *p□<□0.05, **p□<□0.01 or p values, following Brown-Forsythe and Welch ANOVA.

2. **Impact of liver-specific SMN depletion in liver function.** A. Representative images of H&E (top row, scale bar 100 μm) and Oil Red-O (bottom row, scale bar 50 μm) stained liver sections from $Smn^{2B/+}$, $Smn^{2B/-}$, +/+;$Smn^{2B/F7}$, and $Alb^{Cre/+};Smn^{2B/F7}$ mice at P19. B. Bar graph shows quantification of liver triglycerides. **C-E**. Immunoblots were performed to assess heme oxygenase (HO, C-C'), transferrin (D-D') and P62 (E-E') protein levels in the liver. α-tubulin was used as a loading control. C'-E' Bar graphs show quantification of HO (C'), transferrin (D'), and P62 (E') levels. F. Bar graph depicts quantification of liver IGF-1. n□≥□3, mean ± SEM. Statistical significance indicated by *p□<□0.05, **p□<□0.01, ***p□<□0.001, following Brown-Forsythe and Welch ANOVA.

3. **Contribution of liver-specific SMN depletion to pancreatic pathology.** A. Representative immunofluorescent images of pancreatic islets stained for glucagon (red) and insulin (green) from $Smn^{2B/+}$, $Smn^{2B/-}$, +/+;$Smn^{2B/F7}$, and $Alb^{Cre/+};Smn^{2B/F7}$ mice at P19. Scale bar 50 μm. B. Bar graph shows quantification of insulin-positive cells relative to the total number of DAPI-positive cells within the pancreatic islet. C. Bar graph depicts non-fasting blood glucose levels across different genotypes. D-E. Bar graphs illustrate non-fasting plasma levels of insulin (D) and C-peptide (E). F. Bar graph shows quantification of glucagon-positive cells relative to the total number of DAPI-positive cells within the pancreatic islet. G-J. Bar graphs depict non-fasting plasma levels of glucagon (G), active GLP-1 (H), pancreatic polypeptide (I) and active amylin (J). n□≥□3, mean ± SEM. Statistical significance indicated by *p□<□0.05, **p□<□0.01, ***p□<□0.001, following Brown-Forsythe and Welch ANOVA.

4. **Impact of liver-specific SMN depletion on motor neuron cell body numbers.** A. Representative images of lumbar spinal cord anterior horns stained for ChAT (red) and DAPI (blue) from $Smn^{2B/+}$, $Smn^{2B/-}$, +/+;$Smn^{2B/F7}$, and $Alb^{Cre/+};Smn^{2B/F7}$ mice at P19. B. Bar graph shows quantification of motor neuron cell body numbers. n□≥□3, mean ± SEM. Statistical significance indicated by **p□<□0.01, ***p□<□0.001, following Brown-Forsythe and Welch ANOVA. Scale bar = 50 μm.

5. **Impact of liver-specific SMN depletion on neuromuscular junction pathology.** A. Representative images of *transversus abdominis* (TVA) muscle stained with bungarotoxin (red), neurofilament (NF) (green) and synaptic vesicle protein 2 (green) from $Smn^{2B/+}$, $Smn^{2B/-}$, +/+;$Smn^{2B/F7}$, and $Alb^{Cre/+}$;$Smn^{2B/F7}$ mice at P19. *Depicts occupied endplate, whereas **depicts normal neurofilament distribution; arrowheads show NF accumulation and arrows show unoccupied endplate/denervation. B-C. Bar graphs show quantification of neurofilament accumulation (B) and endplate occupancy (C). n = 3, mean ± SEM. Statistical significance indicated by $**p < 0.01$, $***p < 0.001$, following Brown-Forsythe and Welch ANOVA. Scale bar = 50 μm.

6. **Impact of liver-specific SMN depletion on muscle fiber size and distribution.** A. Representative images of H&E-stained *tibialis anterior* muscle sections from $Smn^{2B/+}$, $Smn^{2B/-}$, +/+;$Smn^{2B/F7}$, and $Alb^{Cre/+}$;$Smn^{2B/F7}$ mice at P19. B. Bar graph shows quantification of muscle fiber cross-sectional area. C. Graph demonstrating frequency of muscle fiber size across different genotypes. n ≥ 3, mean ± SEM. Statistical significance indicated by $**p < 0.01$, following Brown-Forsythe and Welch ANOVA. Scale bar = 20 μm.

7. **Consequences of liver-specific SMN depletion to early adulthood liver and pancreatic pathology**. A. Representative images of H&E (top row) and Oil Red-O (bottom row) stained liver sections from $Smn^{2B/+}$, +/+;$Smn^{2B/F7}$, and $Alb^{Cre/+}$;$Smn^{2B/F7}$ mice at P60. Scale bar 100 μm. B. Representative immunofluorescent images of pancreatic islets stained for glucagon (red) and insulin (green) from $Smn^{2B/+}$, +/+;$Smn^{2B/F7}$, and $Alb^{Cre/+}$;$Smn^{2B/F7}$ mice at P60. Scale bar 50 μm. C. Bar graph shows the quantification of insulin-positive cells relative to the total number of DAPI-positive cells within the pancreatic islet. D. Bar graph depicts non-fasting blood glucose levels from P60 mice across different genotypes. E-F. Bar graphs illustrate non-fasting plasma levels of insulin (E) and C-peptide (F). G. Bar graph shows quantification of glucagon-positive cells relative to the total number of DAPI-positive cells within the pancreatic islet. H-K. Bar graphs depict non-fasting plasma levels of glucagon (H), active GLP-1 (I), pancreatic polypeptide (J) and active amylin (K). n ≥ 3, mean ± SEM. Samples were analyzed using Brown-Forsythe and Welch ANOVA, and no statistically significant differences were observed.

8. **Contribution of liver-specific SMN depletion to major adipocyte and gastrointestinal hormones at P19 and P60**. Panels A-B and G-H show bar graphs depicting non-fasting plasma levels of adipocyte-secreted hormones leptin (A, G) and resistin (B, H) in P19 (A-B) and P60 (G-H) mice across different genotypes. Panels C-F and I-L illustrate non-fasting plasma levels of gastrointestinal-secreted hormones, including ghrelin (C, I), gastric inhibitory polypeptide (D, J), peptide YY (E, K), and secretin (F, L) in P19 (C-F) and P60 (I-L) mice. n ≥ 3, mean ± SEM. Statistical significance is indicated by $*p < 0.05$, $**p < 0.01$, following Brown-Forsythe and Welch ANOVA.

9. **Impact of liver-specific SMN depletion on motor function**. A. Schematic representation of experimental design. The righting reflex test was conducted from P7 to P13, the inverted mesh grip test from P13 to P25, and the pen test from P19 to P25. Assessments were performed every two days. Weight was measured every two days until day 30, and then weekly until day 60. Animal welfare was monitored throughout the 60-day period during

weight measurements. B. Kaplan–Meier survival curve comparing *Alb*$^{Cre/+}$;*Smn*$^{2B/F7}$ and +/+;*Smn*$^{2B/F7}$ mice up to 60 days. C, E-G. Graphs show weight (C), righting reflex (E), inverted mesh grip (F) and pen test (G). n = 5 per genotype, mean ± SEM. B: Kaplan–Meier survival analysis; C, E-G: two-way ANOVA, followed by Šídák's method. D. Percentage weight gain at P60, normalized to basal weight at P7. n = 5 per genotype, mean ± SEM, two-tailed unpaired Student's t-test.

Supp. Fig. 1. Cre expression across different tissues. A-B. Representative immunofluorescent images of liver, pancreas and spinal cord at P19 (A) and liver at P60 (B), stained for Cre (red) and counterstained for DAPI (blue, nuclei) from +/+;*Smn*$^{2B/F7}$, and *Alb*$^{Cre/+}$; *Smn*$^{2B/F7}$ mice. Scale bar 50 μm. n=3 per group.

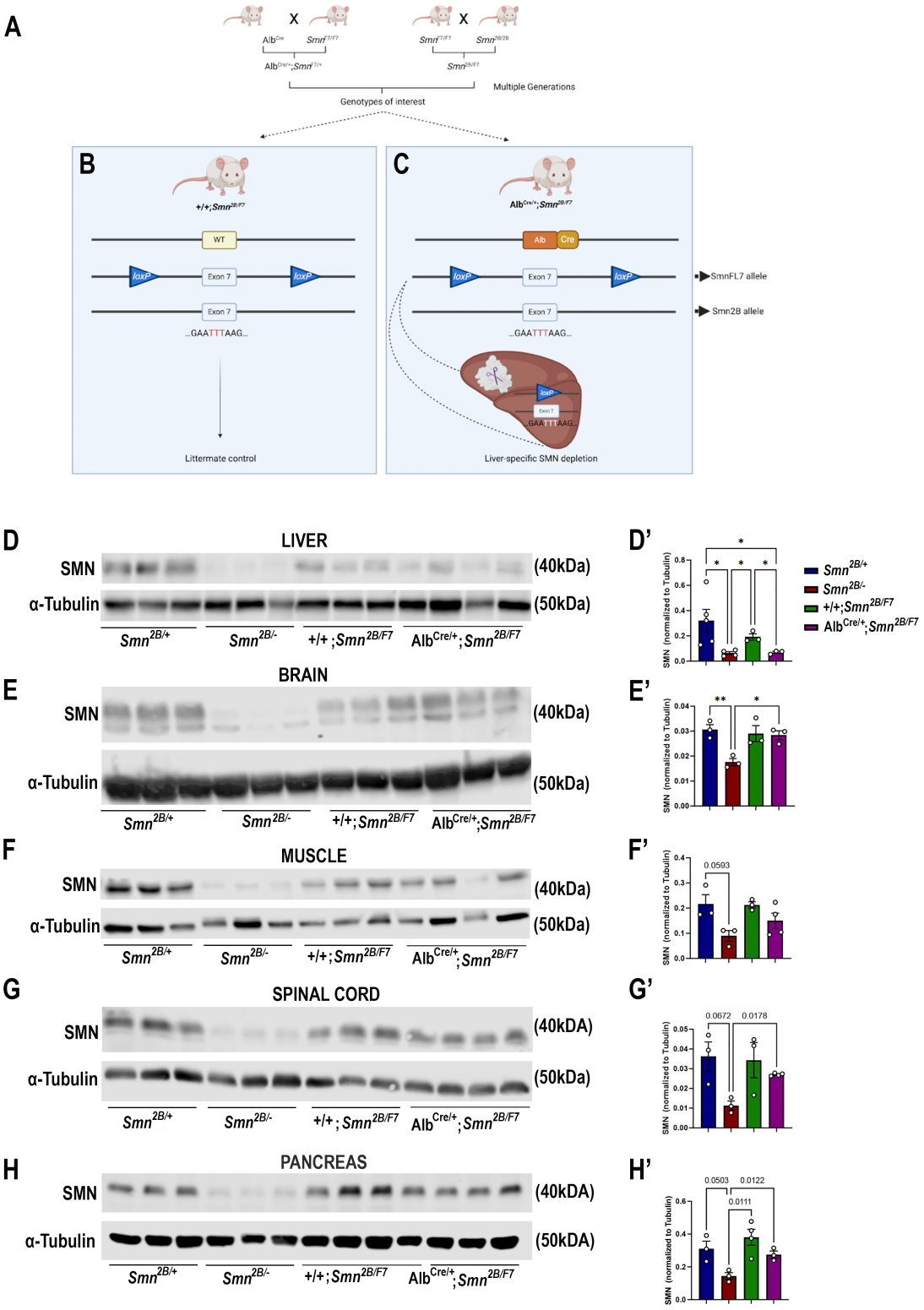
A
Multiple Generations
Genotypes of interest
B
WT
loxP
Exon 7
...GAATTTAAG...
Littermate control
C
Alb
Cre
SmnFL7 allele
Smn2B allele
Liver-specific SMN depletion
D
LIVER
SMN
α-Tubulin
(40kDa)
(50kDa)
D'
E
BRAIN
E'
F
MUSCLE
F'
G
SPINAL CORD
(40kDA)
G'
H
PANCREAS
H'
SMN (normalized to Tubulin)

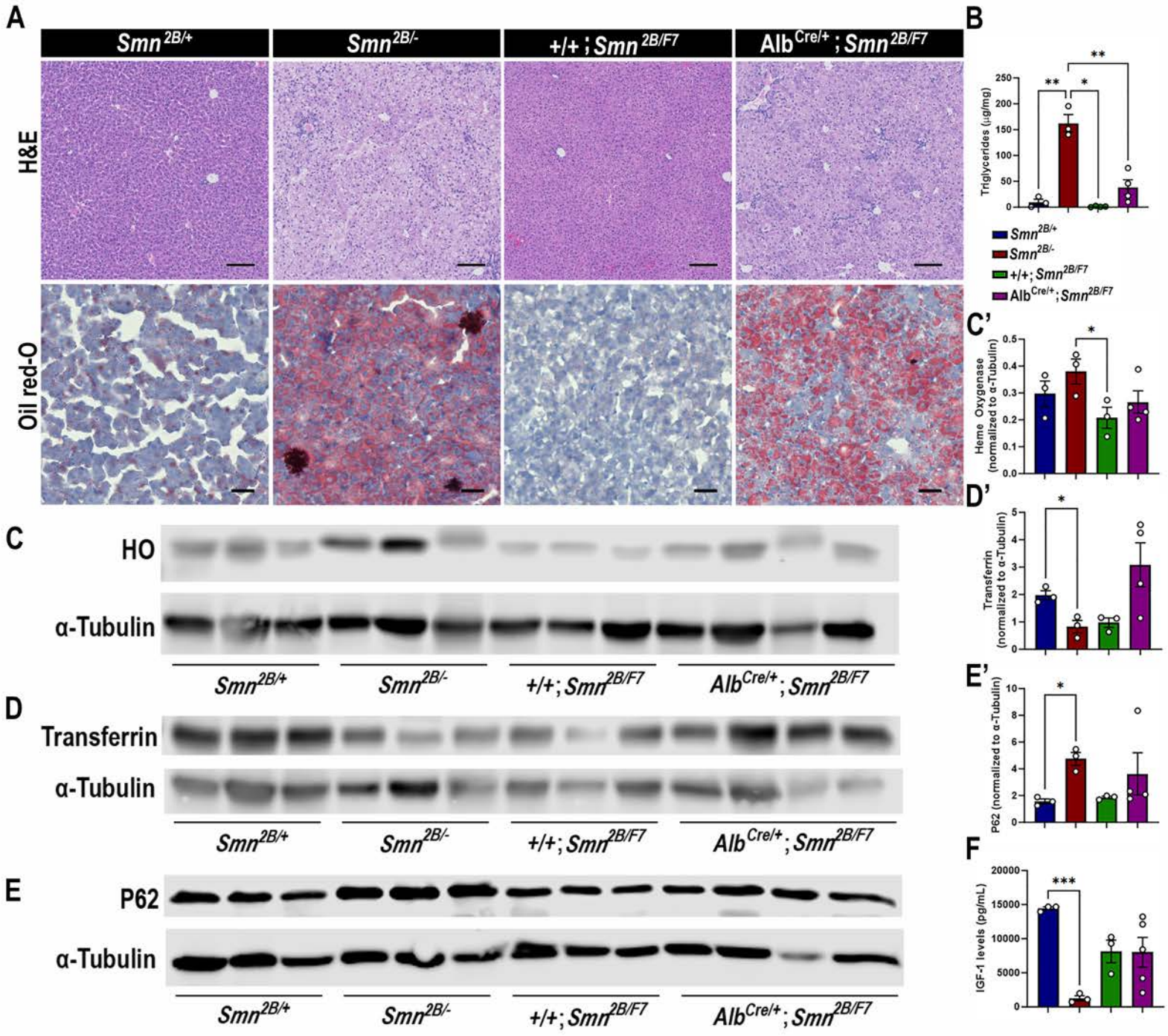
A
Smn 2B/+
Smn 2B/-
+/+ ; Smn 2B/F7
Alb Cre/+ ; Smn 2B/F7
H&E
Oil red-O
B
Triglycerides (µg/mg)
Smn 2B/+
Smn 2B/-
+/+; Smn 2B/F7
Alb Cre/+; Smn 2B/F7
C'
Heme Oxygenase (normalized to α-Tubulin)
D'
Transferrin (normalized to α-Tubulin)
E'
P62 (normalized to α-Tubulin)
F
IGF-1 levels (pg/mL)
C
HO
α-Tubulin
D
Transferrin
α-Tubulin
E
P62
α-Tubulin

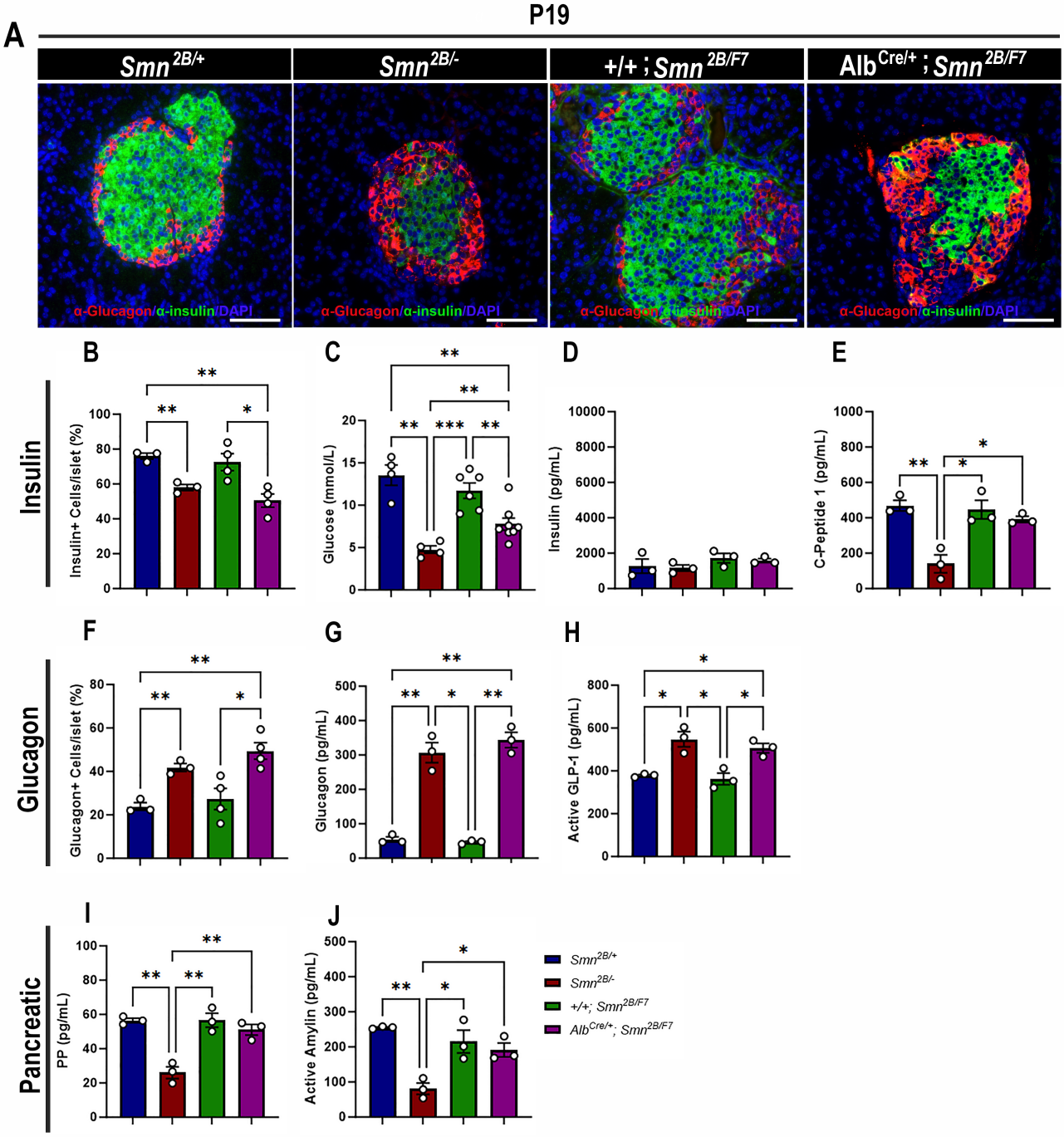
A
P19
Smn 2B/+
Smn 2B/-
+/+ ; Smn 2B/F7
Alb Cre/+ ; Smn 2B/F7
α-Glucagon/α-insulin/DAPI
Insulin
Glucagon
Pancreatic
B
Insulin+ Cells/islet (%)
C
Glucose (mmol/L)
D
Insulin (pg/mL)
E
C-Peptide 1 (pg/mL)
F
Glucagon+ Cells/islet (%)
G
Glucagon (pg/mL)
H
Active GLP-1 (pg/mL)
I
PP (pg/mL)
J
Active Amylin (pg/mL)
Smn 2B/+
Smn 2B/-
+/+; Smn 2B/F7
Alb Cre/+; Smn 2B/F7

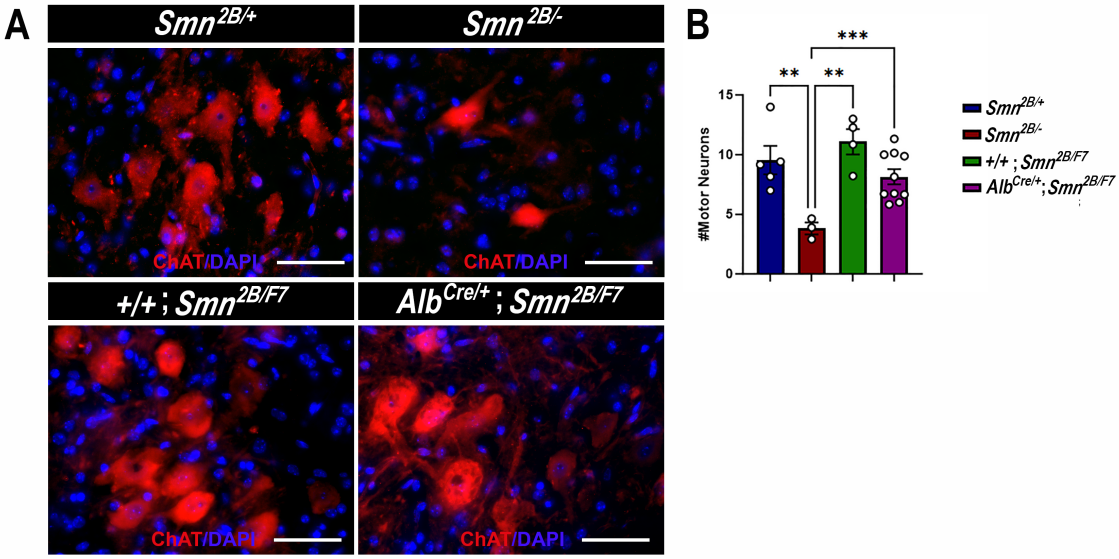
A
Smn2B/+
Smn2B/-
+/+ ; Smn2B/F7
AlbCre/+ ; Smn2B/F7
ChAT/DAPI
ChAT/DAPI
ChAT/DAPI
ChAT/DAPI
B
***
**
**
#Motor Neurons
15
10
5
0
Smn2B/+
Smn2B/-
+/+ ; Smn2B/F7
AlbCre/+; Smn2B/F7

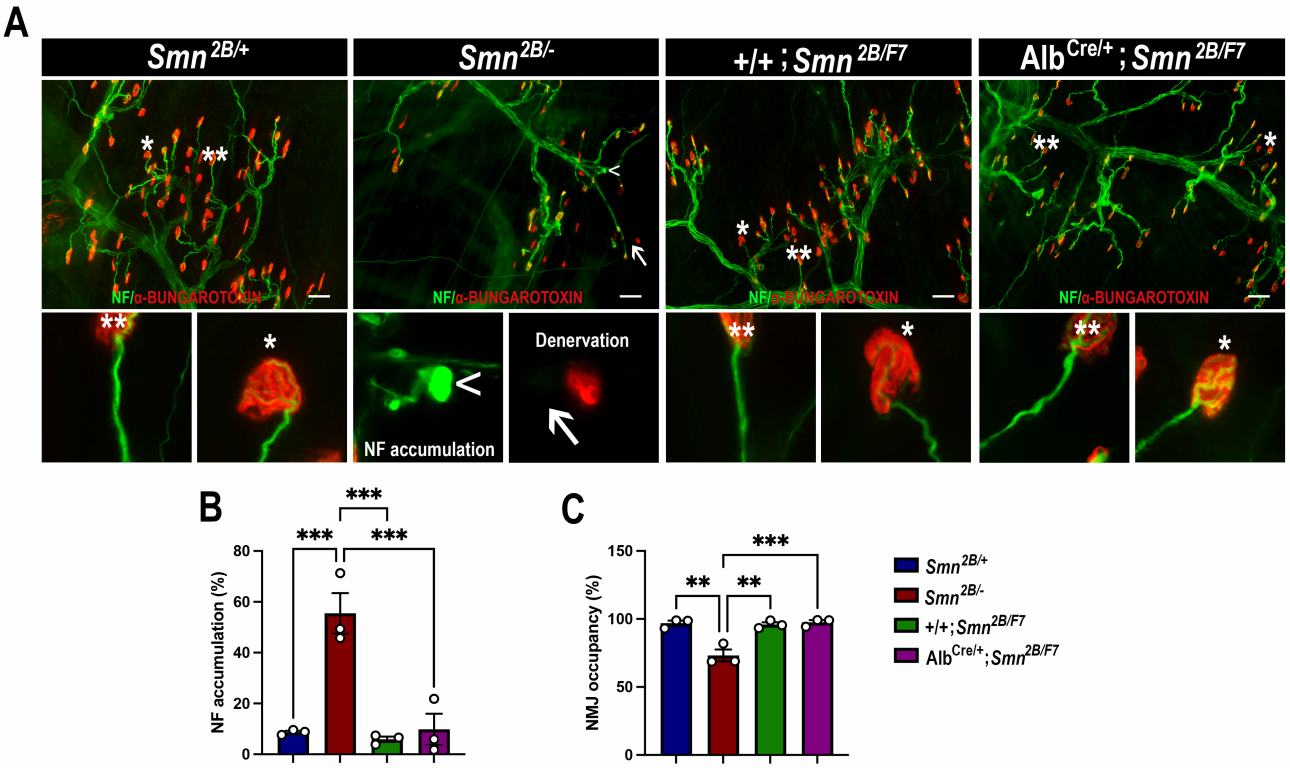
A
Smn 2B/+
Smn 2B/-
+/+ ; Smn 2B/F7
Alb Cre/+ ; Smn 2B/F7
NF/α-BUNGAROTOXIN
NF/α-BUNGAROTOXIN
NF/α-BUNGAROTOXIN
NF/α-BUNGAROTOXIN
Denervation
NF accumulation
B
NF accumulation (%)
80
60
40
20
0
***
***
***
C
NMJ occupancy (%)
150
100
50
0
***
**
**
Smn 2B/+
Smn 2B/-
+/+; Smn 2B/F7
Alb Cre/+; Smn 2B/F7

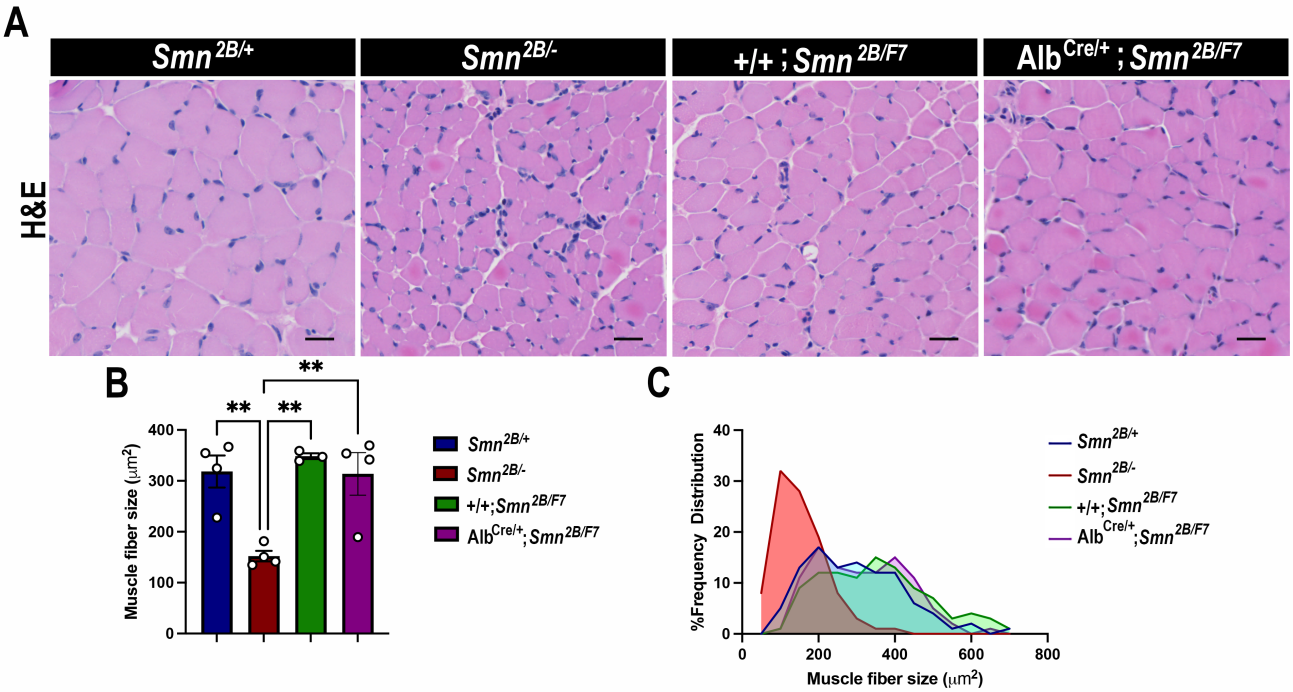
A
Smn2B/+
Smn2B/-
+/+ ; Smn 2B/F7
AlbCre/+ ; Smn2B/F7
H&E
B
**
**
**
Muscle fiber size (μm2)
400
300
200
100
0
Smn2B/+
Smn2B/-
+/+;Smn2B/F7
AlbCre/+;Smn2B/F7
C
%Frequency Distribution
40
30
20
10
0
0
200
400
600
800
Muscle fiber size (μm2)
Smn2B/+
Smn2B/-
+/+;Smn2B/F7
AlbCre/+;Smn2B/F7

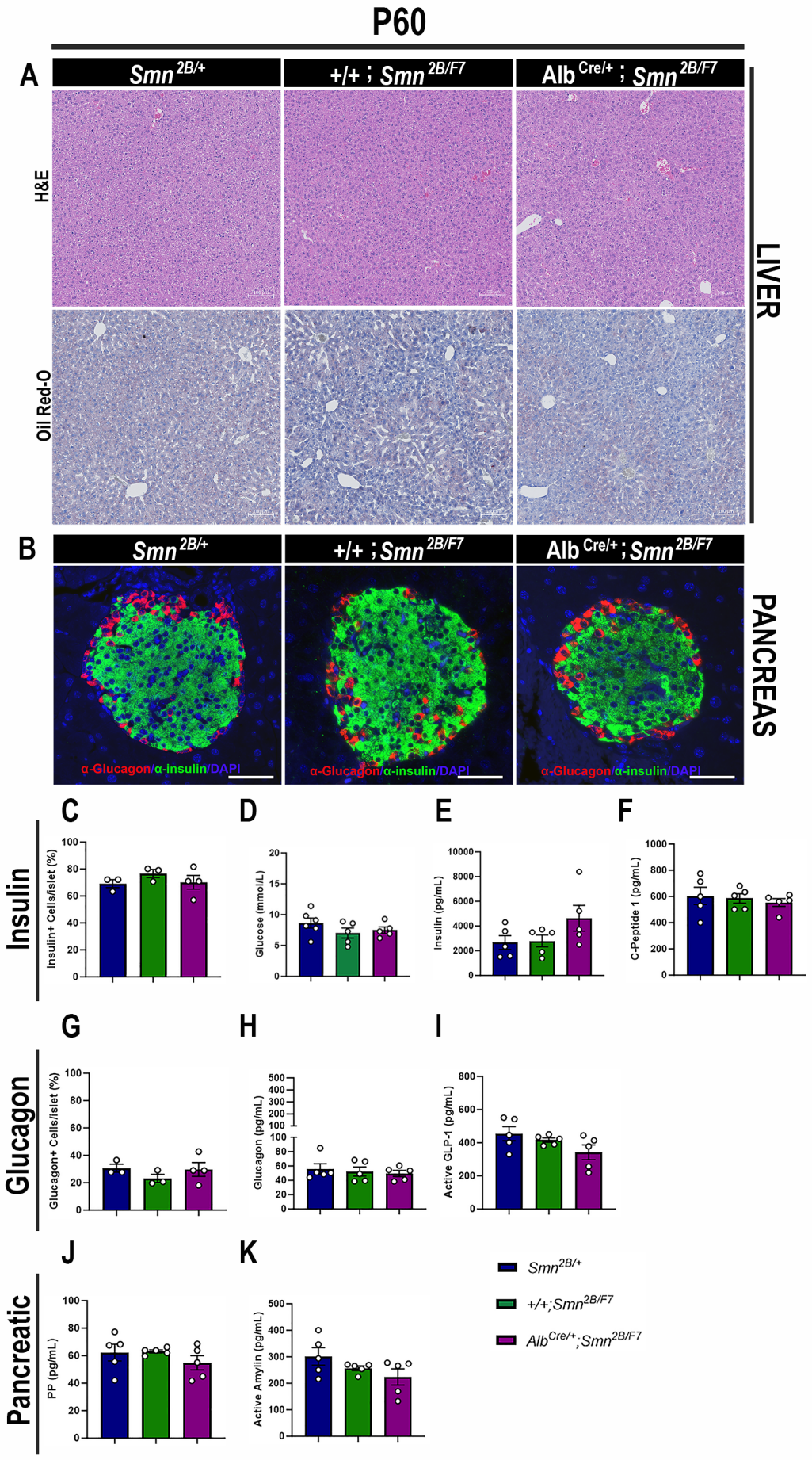
P60
A
Smn 2B/+
+/+ ; Smn 2B/F7
Alb Cre/+ ; Smn 2B/F7
H&E
Oil Red-O
LIVER
B
PANCREAS
α-Glucagon/α-insulin/DAPI
C
D
E
F
Insulin
Insulin+ Cells/islet (%)
Glucose (mmol/L)
Insulin (pg/mL)
C-Peptide 1 (pg/mL)
G
H
I
Glucagon
Glucagon+ Cells/islet (%)
Glucagon (pg/mL)
Active GLP-1 (pg/mL)
J
K
Pancreatic
PP (pg/mL)
Active Amylin (pg/mL)
Smn2B/+
+/+;Smn2B/F7
AlbCre/+;Smn2B/F7

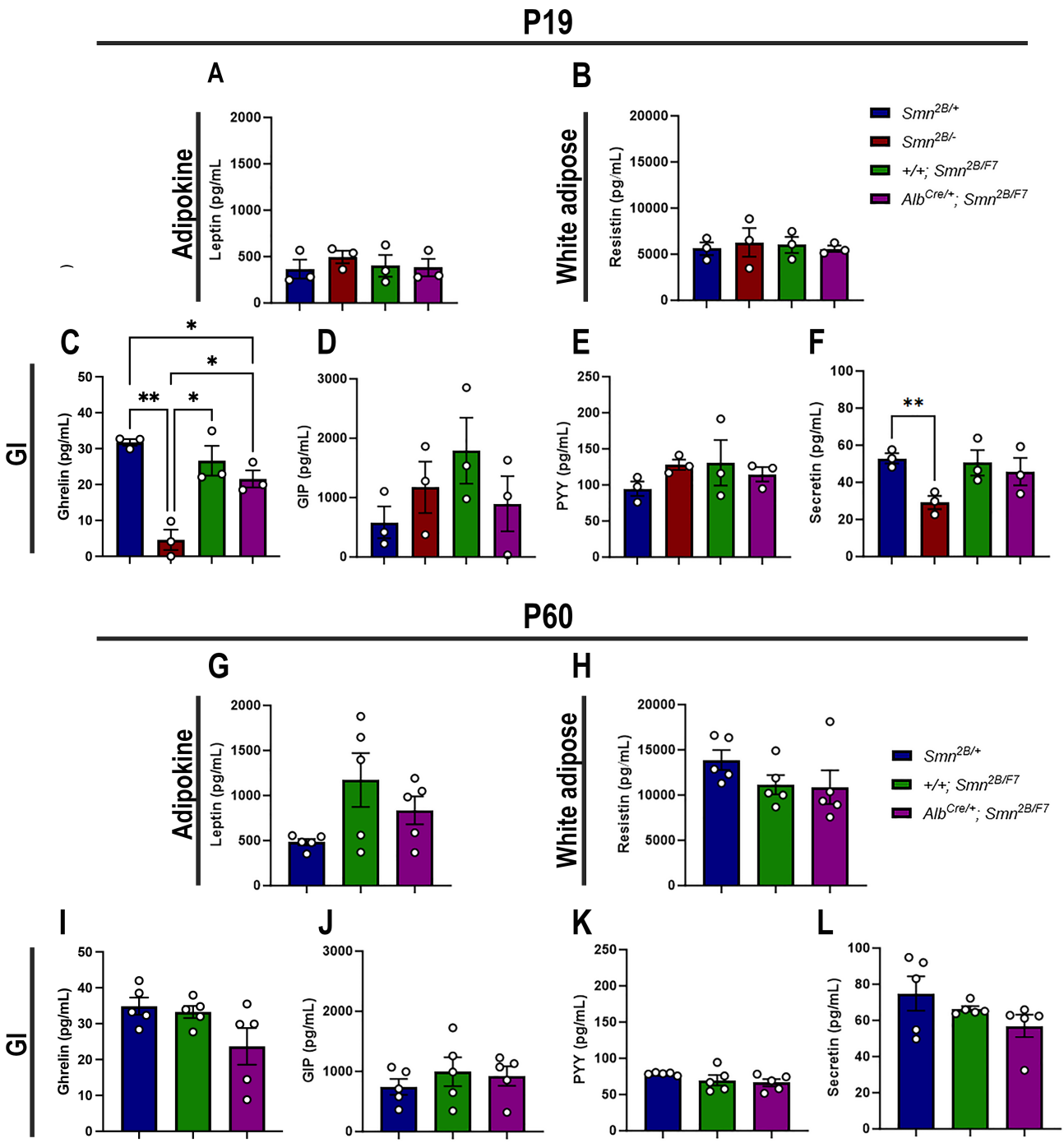
P19
A
B
Adipokine
Leptin (pg/mL
White adipose
Resistin (pg/mL)
Smn2B/+
Smn2B/-
+/+; Smn2B/F7
AlbCre/+; Smn2B/F7
C
D
E
F
GI
Ghrelin (pg/mL)
GIP (pg/mL)
PYY (pg/mL)
Secretin (pg/mL)
P60
G
H
Adipokine
Leptin (pg/mL)
White adipose
Resistin (pg/mL)
Smn2B/+
+/+; Smn2B/F7
AlbCre/+; Smn2B/F7
I
J
K
L
GI
Ghrelin (pg/mL)
GIP (pg/mL)
PYY (pg/mL)
Secretin (pg/mL)

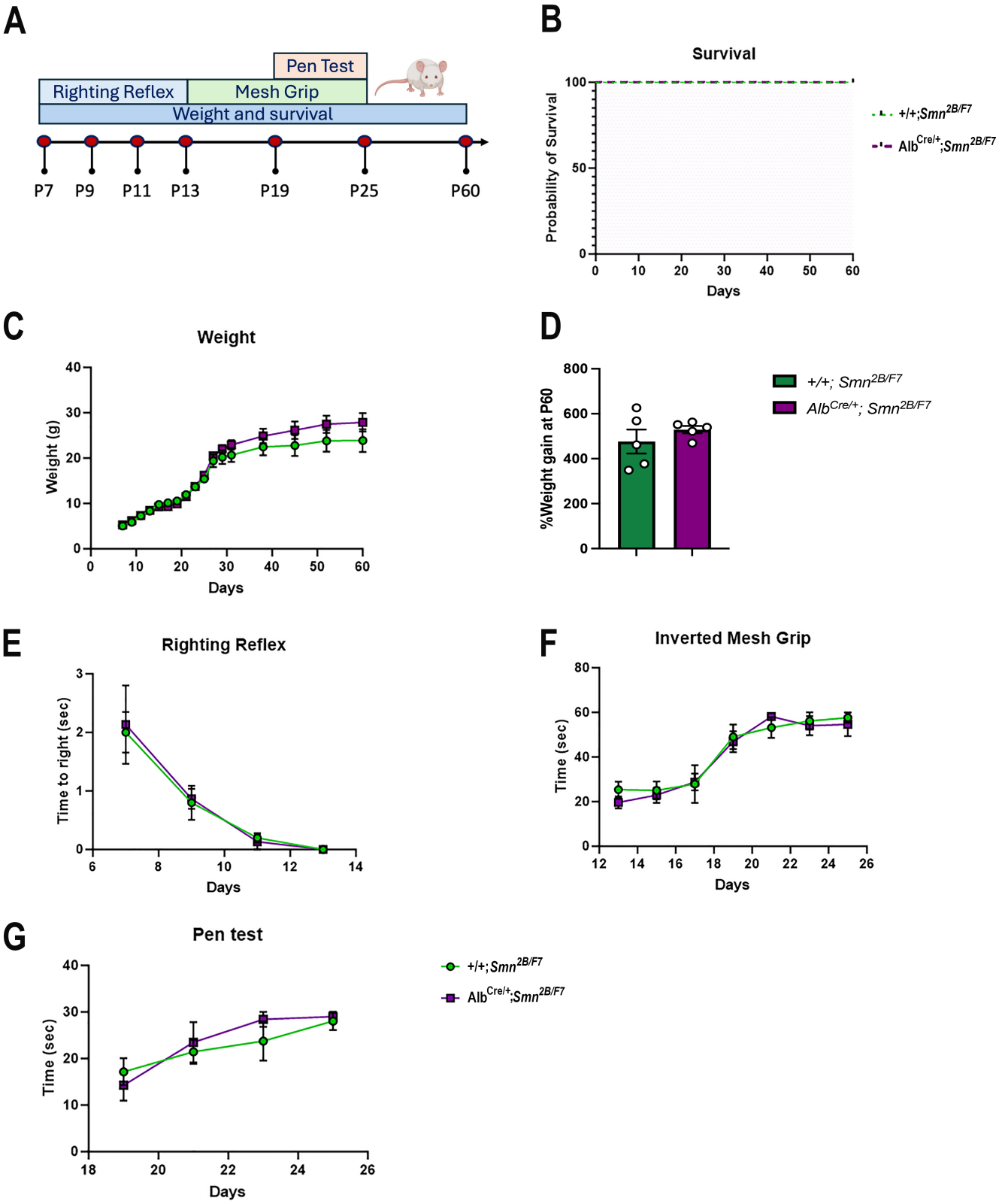
A
Pen Test
Righting Reflex
Mesh Grip
Weight and survival
P7
P9
P11
P13
P19
P25
P60
B
Survival
Probability of Survival
Days
+/+;Smn2B/F7
AlbCre/+;Smn2B/F7
C
Weight
Weight (g)
Days
D
%Weight gain at P60
+/+; Smn2B/F7
AlbCre/+; Smn2B/F7
E
Righting Reflex
Time to right (sec)
Days
F
Inverted Mesh Grip
Time (sec)
Days
G
Pen test
Time (sec)
Days
+/+;Smn2B/F7
AlbCre/+;Smn2B/F7